

Radio-Frequency Linear Analysis and Optimization of Silicon Photonic Neural Networks

Eric C. Blow,* Simon Bilodeau, Weipeng Zhang, Thomas Ferreira de Lima, Joshua C. Lederman, Bhavin Shastri, and Paul R. Prucnal

Broadband analog signal processors utilizing silicon photonics have demonstrated a significant impact in numerous application spaces, offering unprecedented bandwidths, dynamic range, and tunability. In the past decade, microwave photonic techniques have been applied to neuromorphic processing, resulting in the development of novel photonic neural network architectures. Neuromorphic photonic systems can enable machine learning capabilities at extreme bandwidths and speeds. Herein, low-quality factor microring resonators are implemented to demonstrate broadband optical weighting. In addition, silicon photonic neural network architectures are critically evaluated, simulated, and optimized from a radio-frequency performance perspective. This analysis highlights the linear front-end of the photonic neural network, the effects of linear and nonlinear loss within silicon waveguides, and the impact of electrical preamplification.

1. Introduction

Microwave photonic (MWP) systems leverage the large fractional bandwidth between radio-frequency (RF)-modulated signals and optical carriers to perform analog processing tasks at low latency and high dynamic range.^[1,2] Using wavelength division multiplexing, this technological platform enables simultaneous analog processing of the entire modern wireless spectrum at the front-

end of receivers. Historically, the caveat of MWP systems has been poor RF performance with respect to signal link loss and noise figure, which without optimization can frequently disqualify MWP systems from telecommunication applications.^[3,4] Monolithic integration of MWP systems is leveraged to help mitigate these RF concerns by minimizing coupling losses between optical components and significantly reducing size, weight, power, and cost compared to discrete optical systems.^[5]

In the early 2010s, research groups began to use the silicon MWP platform to perform machine learning processing tasks.^[6–9] Although this is not the first attempt at neuromorphic photonics, the combination of these modern platforms offers a promising pathway toward large-


scale integrated solutions compared to free-space optical neural networks.^[10,11] As these fields continue to develop,^[12] their convergence enables next-generation processors, capable of high-bandwidth machine learning processing at the edge.

Silicon photonic neural networks (PNNs) have recently been successfully implemented to address high-speed RF applications. Although silicon PNNs are highly general and applicable to many high-speed real-time processing tasks, the two most prevalent and recent examples of silicon PNNs are with respect to RF fingerprinting^[13,14] and nonlinear dispersion compensation within long-haul communication lines.^[15] While successful in its implementation, the performance of the PNN with respect to these tasks was limited in scope by the RF performance of the system. For example, the RF fingerprinting task could only successfully classify a transmitter if it operates within a wireless environment with a signal-to-noise ratio (SNR) of at least 15 dB.^[14] The minimum SNR required for classification is a product of the difficulty of classification and the signal degradation caused by photonic processing, which in these preliminary systems was unnecessarily high. An SNR requirement limits the scope of classification to high-quality wireless channels. The previously implemented PNN architectures were not designed with RF performance prioritized. Although RF-specific experimental data is not provided within the aforementioned references, these systems would have exhibited high noise figures.^[14,15] From the analysis completed within this article, estimated noise figures upwards of 40 dB would be expected. The detailed analysis and simulation provided in later sections result in improved silicon PNN architectures with respect to noise figure reduction. This improvement

E. C. Blow, S. Bilodeau, W. Zhang, J. C. Lederman, P. R. Prucnal
Department of Electrical and Computer Engineering
Princeton University
Princeton, NJ 08540, USA
E-mail: ecb10@princeton.edu

E. C. Blow, T. Ferreira de Lima
Optical Networking & Sensing
NEC Laboratories America
Princeton, NJ 08540, USA

B. Shastri
Department of Physics
Engineering Physics & Astronomy
Queen's University
Kingston, Ontario K7M 3N6, Canada

 The ORCID identification number(s) for the author(s) of this article can be found under <https://doi.org/10.1002/adpr.202300306>.

© 2024 The Authors. Advanced Photonics Research published by Wiley-VCH GmbH. This is an open access article under the terms of the Creative Commons Attribution License, which permits use, distribution and reproduction in any medium, provided the original work is properly cited.

DOI: 10.1002/adpr.202300306

enables photonic-enhanced machine learning without the caveat of requiring high-SNR RF environments. In addition to SNR considerations, later sections of this article include RF dynamic range analysis of silicon PNNs and explore techniques to maintain weighting accuracy at high operating frequencies with broad bandwidths.

2. Silicon Photonic Neural Networks

The analysis in this article will be limited to the broadcast and weight silicon PNN architectures.^[9,15] Alternative PNN architectures, such as Mach-Zehnder interferometer mesh networks,^[16] would also benefit from RF analysis and optimization, but the differences in optical loss of these two architectural types would need to be accounted for. As shown in **Figure 1**, the broadcast and weight silicon PNN comprises a linear optical front-end and a nonlinear optical back-end. The linear processing requirement of a neural network is positive and negative weighted summation, while the nonlinear processing of a neural network is an application-specific activation function responsible for decision-making. Between the two optical subsystems, an electrical link enables transimpedance amplification. All three subsystems have been demonstrated on a silicon photonic integrated circuit (PIC).^[6,17,18]

In this architecture, the weighting is accomplished using a silicon microring resonator (MRR) weight bank.^[6] A MRR weight bank contains N number of MRRs with unique resonances corresponding to N unique optical carrier wavelengths modulated by RF input signals. The difference between resonance of the MRR and input wavelength determines the amount of light that couples into the ring and transitions from the input port to the drop port of the MRR. A thermal metal heater is cointegrated directly above the silicon MRR. As heat is generated by driving the embedded heater, the resonance of these devices begins to shift due to the thermo-optic effect within the silicon waveguide. By tuning the resonance of the MRR from on resonance to off resonance with respect to the input wavelength, an optical signal can be

weighted between 0 and 1 while the drop port is observed. The key to this architecture is that the thru port of the MRR is a complementary output to the drop port. Therefore, by pairing the MRR weight bank with a balanced photodetector (BPD), subtraction of the thru and drop ports occurs, resulting in -1 to $+1$ optical weighting. The summation of all inputs is also accomplished via the BPD, as the speed of this device is much slower than the wavelength of the optical carriers, summing the incident optical signals at the BPD across wavelengths. In-depth literature on implementation and control of these weight banks is shown in refs. [6,7,19,20].

Within the silicon PNN, the nonlinearity processing requirement is achieved by biasing MRR modulator within the nonlinear region of the modulation transfer function^[21] and driving this modulator with the output of the linear front-end. The silicon photonic modulator neuron has demonstrated a variety of relevant transfer functions to machine learning tasks, specifically sigmoids, rectified linear units, a radial basis function, and quadratic functions.^[17]

The combination of the linear front-end and nonlinear back-end creates an optical-electrical-optical (O-E-O) link per photonic neuron. The O-E-O link enables optical pumping in each layer, which could introduce an effective optical gain even with passive transimpedance.^[22] This can be further enhanced with active electronics, either implemented directly in the silicon photonic platform^[18] or through cointegrated high-speed complementary metal-oxide-semiconductor electronics.^[23] The access to amplification within each photonic layer enables the potential to reach unity gain and therefore scale the network without signal degradation.^[22] Scaling is a critical advantage of this architecture, compared to all-optical approaches.^[16]

3. Demonstration of Wideband Linear Optical Weight Bank

Previous reporting of silicon weight banks has shown variation in weighting over narrow bandwidths,^[24] which leads to a limitation in input instantaneous bandwidth of the silicon PNN to 100s of

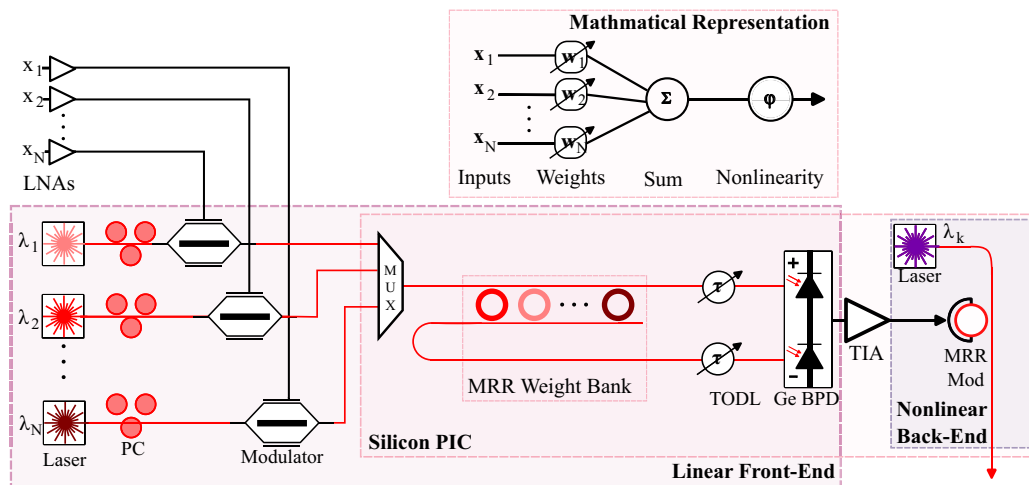


Figure 1. Mathematical representation of neuromorphic processing requirements (top subfigure) and correlating schematic demonstrating the photonic implementation of these requirements into a broadcast and weight architecture. The schematic highlights the linear front-end and nonlinear back-end, as well as highlighting which processing is computed typical on the silicon PIC. PC = polarization controller, MRR = microring resonator, TODL = tunable optical delay line, BPD = balanced photodetector, TIA = transimpedance amplifier.

MHz. This variation in weighting was the result of high-quality factor MRR optical resonances. Within the previous work,^[24] the full width half maximum (FWHM) was equivalent to 9.7 GHz, which limits the bandwidth of linear weighting. Within this demonstration, 11.3 μm -radius silicon MRRs were designed to have a lower Q-factor and a broader resonance, with FWHM of 43.37 GHz. These experimentally measured rings demonstrated a significant increase in the RF weighting bandwidth, with a 3 dB bandwidth of 4.7 GHz and a 6 dB bandwidth of 9.5 GHz. Furthermore, these results demonstrated a low weight variation of <0.1 dB. Disadvantages to broadening include the reduction in the number of possible channels before requiring reuse of wavelengths, as well as a larger tuning range requirement to cover the weighting range. If the free spectral range (FSR) of the resonator structure is less than the bandwidth of the optical C-band, the maximum number of channels is defined as the FSR divided by the FWHM. If not, the number of channels is the spectral width of the C-band divided by the FWHM. The thermal tuning of the rings has a fixed $\Delta\lambda/\Delta T$ and, therefore, a larger FWHM requires a linear scaling of the thermal power required to tune the MRR weight.

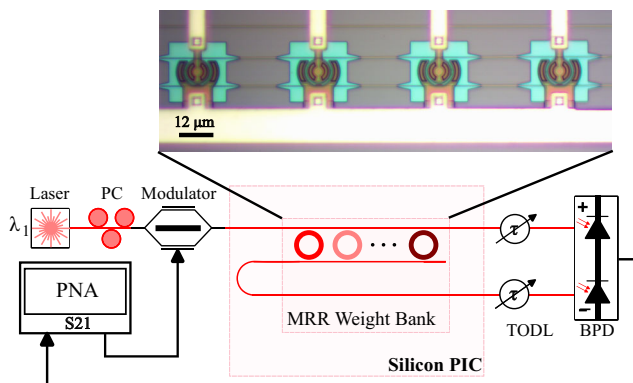


Figure 2. Experimental setup for broadband linear front-end weighting. Including micrograph of silicon photonic weight bank used within the experiment. PNA = portable network analyzer, PC = polarization controller, MRR = microring resonator, TODL = tunable optical delay line, BPD = balanced photodetector.

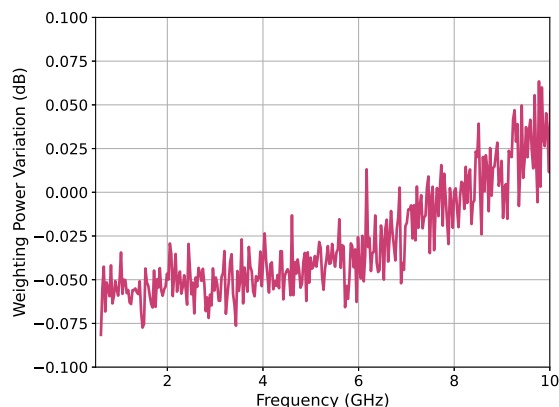
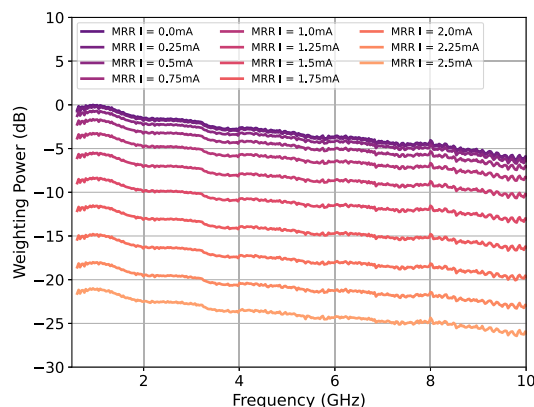


Figure 3. RF transfer function, S21, results of MRR as a function of applied current from 0.0 to 2.5 mA, corresponding to a neural network weight tuned from on-resonance to off-resonance (left). Difference in the transfer function of each weighting step showing the bandwidth dependence of the weight as a function of frequency and applied weight (right).

As shown in **Figure 2**, a microwave network analyzer, Keysight N5222A PNA, was connected to the silicon weight bank through an off-chip 10 GHz Mach-Zehnder modulator (MZM) and a BPD. The wavelength of the tunable laser source was set to 1551 nm, near the edge of the MRR resonance which was centered at 1551.7 nm. The optical carrier was modulated via the MZM and then vertically coupled to the silicon photonic chip through grating couplers. The signal was weighted by the MRR and then coupled off-chip to two tunable optical delay lines (TODL). The TODLs are used for delay and phase matching of the thru port and drop port optical paths before subtraction at the BPD. The weighting was then swept by adjusting the amount of current applied to the embedded resistive heater.^[7,20]

The measured S21, shown in **Figure 3a**, demonstrated a 3 dB weighting bandwidth of 4.7 GHz and was tested for broadband weighting from -1 to $+1$. The varying trace color from purple to orange of **Figure 3a** represents the S21 of linear front-end of the neural network while linearly sweeping the MRR control current from fully on-resonance to off-resonance. The weighted signals were subtracted to measure the variation in weighting as a function of frequency between all different possible weighting values, as shown in **Figure 3b**. Variation in weighting as a function of bandwidth would limit the instantaneous bandwidth of RF input signals that can be processed simultaneously. This measurement demonstrates the broadband operation of silicon weight banks and the design trade-off between instantaneous processing bandwidth and channel density.

4. Weighting Accuracy at High Operating Frequencies

As the operating frequency of the silicon PNN linear front-end increases, additional requirements become relevant to achieve precise and accurate wideband weighting. The two optical paths of silicon weight banks must be matched in amplitude, delay, and phase.^[25] If mismatched, there will be a limitation to the accuracy of the weighting achieved by subtraction as shown in Equation (1). The amplitude mismatch term, $\Delta\alpha$, is the primary mechanism used to generate the weight, w_i . The initial amplitude mismatch between the two optical paths can be calibrated

within the MRR control. Within demonstrations of a single MRR weight-bank operation, such as presented in this article, delay and amplitude matching are compensated with off-chip TODL and variable optical attenuators. The importance of this matching is understated in the literature.

In a fully integrated solution of silicon PNNs, the amplitude mismatch between the two optical transfer functions can still be calibrated with MRR control, but any delay difference must be matched for each weight within each photonic neuron. The effect of phase and delay mismatch, $\Delta\phi$ and $\Delta\tau$, increases proportionally with the operating frequency of the PNN. The proportionality between the weighting variance and the operating frequency is shown experimentally in Figure 3b. The sensitivity to mismatch is maximized when the output of the linear front-end of the silicon neuron is set to zero, implying that the input has no correlation to the output decision. This requirement for precise photonic subtraction is identical to the processing requirements of MWP cancellation systems.^[26] Delay-mismatched weight-bank response results in an interferometric fringe response with spacing equal to integer multiples of the delay mismatch. This fringe response yields operating frequencies where uncorrelated input signals impact the output of the neuron. As a result, high-frequency silicon weight banks require additional delay tuning on thru and drop optical paths to address for mismatch introduced by the add-drop weight bank geometry.

Weight banks with single MRRs introduce a delay difference dependent on the location of the ring because of the inability to match the thru path and drop path for all rings. Double MRR resonators can be implemented to match the optical path length regardless of location. There is a delay mismatch introduced by the difference in effective optical path length as a result of the varied ring geometry required for each channel. Finally, MRRs introduce a phase shift dependent on detuning for each weighting channel. To fully match the effects within these two paths requires a wavelength-sensitive delay for each individual weight. This can be achieved by implementing MRR racetrack delays that have resonances equal to the weights of interest (Figure 4).^[27]

$$w_i X_i = (1 + \Delta\alpha - 2\Delta\alpha \times \cos(i\omega\Delta\phi + \Delta\tau)^2) X_i \quad (1)$$

5. Radio-Frequency Analysis

5.1. Linear Front-End and Nonlinear Back-End

The RF performance analysis within this article will focus on three critical metrics: link loss, noise figure, and spurious-free dynamic range (SFDR). RF link loss is the reduction in RF power

due to the device-under-test (DUT). Noise figure is a metric for quantifying the SNR degradation due to the DUT. SFDR is defined as the power difference between the minimal detectable signal (MDS) and the RF input power when the intermodulation distortion (IMD) products begin to dominate the fundamental signal. Within an optical system, the third-order IMD dominates. The RF analysis within this section builds on the conference proceedings,^[28] which provided basic simulations of neuromorphic photonics without consideration of silicon photonic loss, waveguide nonlinearities, low noise amplification (LNA), nor dynamic range. The foundations of this analysis can be found in primary refs. [3,29–33].

The RF performance of a PNN in its totality is fundamentally limited by the RF performance of a single optical subsystem, the linear front-end of the input layer. The limitation is defined as such because this is the only section of the neural network's processing chain which is intended to operate with a linear transfer function acting on unprocessed analog input signals. A critical result of PNN nonlinear noise analysis from Ferreira de Lima, et al.^[22] showed noise performance conservation of the propagating signals from layer to layer within the PNN due to nonlinear operation. Therefore, the RF performance of the optical linear front-end will determine the SNR range in which input signals can be processed. Achieving cascalability of the PNN after the first linear layer requires compensation for the RF power loss from layer to layer. This can be achieved with an O-E-O electrical gain, as explained in Section 2. RF analysis and optimization can have two significant impacts. First, optimizing and lowering the noise figure of the linear front-end results in a lower SNR requirement of the input signal, extending the application space of neuromorphic photonics. Second, optimizing and lowering the RF power loss of each photonic neural layer reduce the gain requirements of the electrical amplification responsible for compensating this loss in aims to achieve network scalability. Within this article, the analysis perspective is equivalently shifted from the perspective of each neuron, O-E-O, to the perspective of weighted neural interconnections, E-O-E. In this perspective, the electrical input signal is driving the previous modulator neuron, and the weighted output electrical signal is driving the next modulator neuron. All three RF performance metrics highlighted within this analysis share proportionality with the input optical power, and therefore this parameter will be utilized as the independent variable for the simulations.

5.2. Link Loss Analysis

Link loss is defined as the RF power ratio between the input and output of an analog photonic link. The primary causes of loss

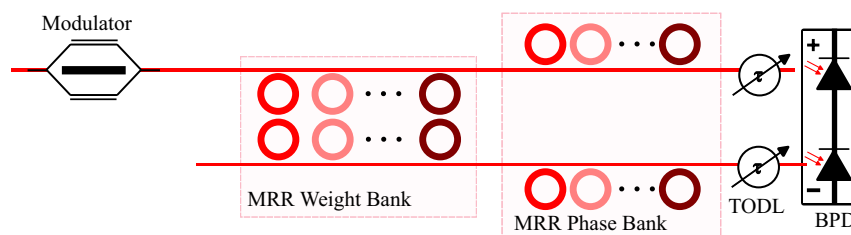


Figure 4. Addition of wavelength-sensitive phase bank for individual channel phase matching to ensure weighting accuracy.

within the linear front-end of the broadcast and weight neural network are inefficiencies of the electrical-to-optical up-conversion (modulation) and optical-to-optical down-conversion (detection). The optical link loss accounts for all insertion losses accrued by processing and optical coupling. Additionally, there are linear and nonlinear losses associated with waveguide propagation. Resonator-based NP architectures are more significantly affected by nonlinear loss because of power buildup within the MRR.^[32] Finally, this analysis will assume passive resistive impedance matching, which introduces a 1/4 loss term, but this could be improved with active impedance matching at the cost of bandwidth. For all layers that follow the input layer, the transimpedance amplifier must exceed the RF loss; otherwise, there will be a scaling limit to the PNN layer depth. Finally, there is loss associated with signal fan-out to multiple neurons.

$$G_{\text{PNN}} = \frac{(G_{\text{Impedance}})(G_{\text{mod}})^2(G_{\text{opt}})^2(G_{\text{Waveguide}})^2}{(G_{\text{MRR}})^2(G_{\text{Detect}})^2} \quad (2)$$

The modulation type, direct or external, of the input layer is a critical architectural choice for the system. Historically, external modulation has been used as the input layer of the PNN.^[12,21] Note the modulation loss terms, Equation (3), and the dependence on the input optical power. The gain of a directly modulated (DM) architecture is independent of optical power, while the gain of an externally modulated (EM) architecture is dependent on the square of optical power. With respect to external modulation, the modulator can be either off-chip, such as a larger lithium niobate efficient modulator at the cost of size, weight, power, and cost (SWaP-c), or on-chip, such as a highly compact silicon modulator. The off-chip modulators allow for longer phase actuation regions with lower-loss waveguides, yielding a higher modulation sensitivity and therefore a lower V_{π} ,^[34] compared to compact silicon modulators.^[35,36] With respect to DM, the modulation efficiency depends on the slope efficiency, s_{LD} , of the directly modulated laser (DML). The bandwidth of DMLs has improved significantly in recent years, with demonstrations of speeds up to 55 GHz,^[37] but is typically inferior to external modulations with respect to this metric. Given the proportional relationship between the modulation sensitivity, V_{π} , and the link gain for an EM system, the input layer modulators of the PNN should be optimized for V_{π} at the cost of physical chip space.

$$G_{\text{DMmod}} = (s_{\text{LD}}) \quad G_{\text{EMmod}} = \left(\frac{P_{\text{opt}} T_{\text{Mod}} R_L \pi}{2V_{\pi}} \right) \quad (3)$$

In this analysis, the optical loss due to processing is defined as the coupling loss and the insertion loss of the MRR weights. An edge coupler with 1.2 dB insertion loss was used for the analysis, as demonstrated by Advanced Micro Foundry.^[36] The insertion loss of the MRR from input to drop port, terminated at BPD, was measured to be 0.2 dB when set fully on resonance.

There are linear and nonlinear waveguide loss mechanisms within silicon photonic waveguides. The linear propagation loss, α_0 , is measured as 1.04 dB cm^{-1} in standard width and thickness strip waveguides^[36] and the length of the waveguide was defined as 2 mm as observed by previously published linear weight banks.^[7] Additional waveguide loss due to on-chip modulator length is also considered. The nonlinear mechanisms within

the waveguide are free carrier absorption (FCA)^[38,39] and two-photon absorption (TPA).^[31] FCA, Equation (4), is dependent on the optical power and the amount of free-carriers, ΔN_e and ΔN_h , within the effective mode area of the waveguide, Area_{FCA} .^[40] TPA is dependent on the material properties of the waveguide, the optical input power, and the effective mode area of the waveguide, Area_{TPA} .^[40] The nonlinear material coefficients for silicon, β_{TPA} and σ_{FCA} , in addition to the carrier life-time, τ_c , determine the material-specific strength of the nonlinear effects and are shown in Table 1 with respect to the transverse electric (TE) mode.

Comprehensive literature on nonlinearities within silicon waveguides can be found in refs. [31,32,40]. The nonlinearities effects computed for this analysis were with respect to a 500 nm silicon-on-insulator strip waveguide. The ordinary differential equation, Equation (5), reflecting the effects of TPA and FCA, was solved over the length of the waveguide and yielded a significant nonlinear loss at 15 dBm optical power. Nonlinear waveguide loss introduces a linear and square loss dependence on optical power, yielding a gain limit for EM links which is asymptotically approached. Additionally, there is an upper threshold of optical power within a silicon waveguide approximately at 33 dBm, where power buildup results in irreparable damage to the silicon waveguide.^[41]

$$G_{\text{FCA}} = 8.5 \times 10^{-18} \Delta N_e + 6.0 \times 10^{-18} \Delta N_h \quad (4)$$

$$\frac{\delta P}{\delta z} = -\alpha_0 P - \alpha_2 P^2 - \alpha_3 P^3 \quad (5)$$

$$\alpha_2 = \frac{\beta_{\text{TPA}}}{\text{Area}_{\text{TPA}}} \quad (6)$$

$$\alpha_3 = \frac{\beta_{\text{TPA}} \sigma_{\text{FCA}} \tau_c}{2 * h\nu \text{Area}_{\text{FCA}}^2} \quad (7)$$

As mentioned previously, resonator-based MWP systems are more sensitive to nonlinear losses due to power buildup within MRRs. The MRR optical spectrum was measured for the silicon weight bank. From this data, FWHM of 348.3 pm, FSR of 8.546 nm, and a finesse of 24.54 were measured. Additionally, a finite-difference time-domain simulation was developed

Table 1. Parameter definition for RF analysis.

Symbol	Metric	Value
P_{in}	Optical power in	Swept 0–25 dBm
T_{mod}	Optical transmission loss of modulator	On-chip 7 dB ^[52] Off-chip 3.5 dB ^[53]
R_L	Load resistance	50 Ω
V_{π}	Voltage required for π phase shift of modulator	On-chip 4 V ^[52] Off-Chip 3.5 V ^[53]
r_{PD}	Photodetector responsivity	1.09 mW mA ⁻¹ ^[43]
s_{LD}	Slope efficiency of laser diode	0.3761 mW mA ⁻¹ ^[54]
RIN	Relative Intensity Noise	–162 dB Hz ⁻¹ ^[54]
β_{TPA}	Silicon TPA coefficient	24.8 cm GW ⁻¹ ^[40,55]
$\sigma_{\text{FCA}} \tau_c$	Silicon FCA coefficient * Silicon Carrier Lifetime	9.71 $\times 10^{-27}$ cm ² s ^[40,55]

utilizing the open-source software MEEP^[42] to estimate the coupling coefficient, r . This resulted in a value of 0.966 for the MRR's point coupler for 1.55 μm optical signals. The measured resonances metrics and the simulated coupling coefficient were used in Equation (8) to calculate a round-trip loss coefficient, a , of 0.91. Finally, these metrics were used in Equation (9) to solve for a power buildup of 4.736 within the MRRs. This buildup factor multiplies the effective optical power inside the MRR's waveguides, and the nonlinearities were simulated over the length of the MRR's circumference, 71 μm . The nonlinear effects within the MRRs cause nonlinear attenuation to begin to dominate the system at lower optical powers. Additionally, at high optical power, these effects increase significantly, resulting in an well-defined optimal operating point for the EM link architectures. Nonlinear effects within the MRRs also lower the optical damage threshold limit by a factor of the power buildup.

$$F = \frac{\text{FSR}}{\text{FWHM}} = \frac{2\pi}{2\text{arccos}\left(\frac{2ar}{1+a^2r^2}\right)} \quad (8)$$

$$B = \frac{a^2(1-r^2)}{1-2\text{arccos}(\phi) + a^2r^2} \quad (9)$$

The detection efficiency depends on the square of responsivity of the on-chip germanium-on-silicon photodetector. A typical on-chip photodetector that operates at up to 40 GHz with a responsivity of 1.09 $\text{A W}^{-1[36,43]}$ was utilized for these simulations.

$$G_{\text{Detect}} = r_{\text{PD}} \quad (10)$$

Note that this analysis and the input optical power term are not considering the fan-out (power reduction from signal splitting) of the input layer. Fan-out manifests itself within the G_{opt} term. The fan-out optical loss will reduce the optical input power before resonator devices, and therefore, the strength of the waveguide nonlinear will set the upper limit of fan-out without performance degradation. At this upper limit, the optical power increased to account for fan-out is attenuated within the waveguide. An estimated adjustment to the new optimal optical power operating point considering fan-out would be to compensate for the optical loss of the fan-out process until this additional power is equivalent to the power build-up factor within the MRR. At this point, increasing optical power will only be absorbed within the waveguide, resulting in a stagnation in optical gain and an inability to compensate for further fan-out.

The link loss analysis was calculated using typical device performance metrics with commercial-of-the-shelf (COTS) and on-chip components available through current silicon photonic foundry process design kits, as shown in Table 1.^[23,36,44,45] Analysis exploring the fundamental limits to the power of weighting, matrix vector multiplication, can be found in ref. [33].

The link loss for five potential PNN linear front-end architectures is shown in Figure 5. The solid curves indicate DM and on/off-chip EM. The novel balanced PNN front-end, dashed curves, will be introduced in later sections. This figure highlights the dramatic impact of nonlinearities within the waveguide and MRR. Without nonlinearities, the link loss for the DM architecture is independent of optical, and the EM architectures only

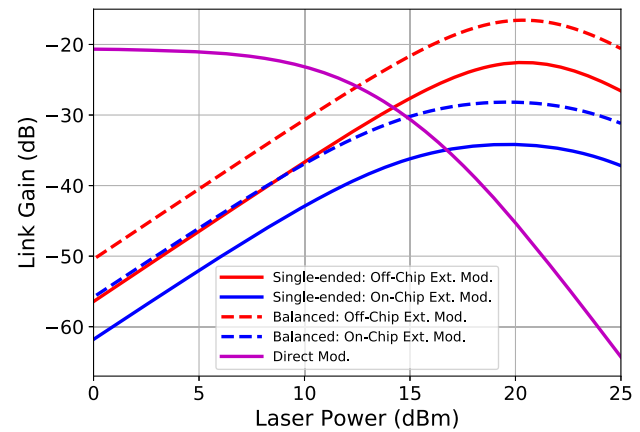


Figure 5. RF link loss of the linear front-end of the PNN as a function of optical power for different modulation architectures. Solid curves are single-ended links while dashed curves are balanced. Purple curve indicates off-chip direct modulation, red curves indicate off-chip external modulation, blue curves indicate on-chip external modulation, and dashed line indicates on-chip modulation.

increase in gain as a function of optical power squared. In this complete RF model of the PNN front-end, all architectures have an optimal optical power input with respect to link loss. Architectures with waveguide nonlinear loss mechanisms but without resonators would result in link loss asymptotically reaching a maximum gain. With resonator buildup loss mechanisms, after exceeding this optimal gain point, increasing optical input power results in excess loss worsening the overall system performance. Increasing the buildup factor within the MRR results in a shift of the optimal operating point to lower optical powers. These results are representative of the MRRs presented in the Experimental Section. The DM PNN architectures perform best at low optical power, 0 dBm, achieving -20.66 dB in link gain. The EM on-chip PNN loss is minimal at 20.4 dBm optical power, achieving -34.17 dB of link gain, and the EM off-chip PNN loss is minimal at 20.4 dBm optical power, achieving -22.56 dB link gain.

5.3. Noise Figure Analysis

Noise figure is an RF performance metric that represents the degradation in SNR due to the device-under-test, in this case the silicon photonic PNN. There are three primary noise sources within analog photonic links: thermal noise, shot noise, and relative intensity noise (RIN).^[3] Note the difference in optical power dependency between these noise sources: Thermal noise is independent, shot noise is linearly proportional, and RIN noise is proportional to the square of optical power at the photodetector. These dependencies create three separate performance regions, depending on which noise term currently dominates the system. The regions are defined with respect to optical power and are strongly dependent on the temperature of the PIC, the noise quality of the laser, and the bandwidth of the photodetector.^[29] The RF noise figure is shown in Equation (12). Substituting the PNN gain term for the EM or DM specific gain term results in a noise figure equation dependent on the architecture.

$$F = \frac{N_{out}}{GN_{in}} \quad (11)$$

$$F_{PNN} = 1 + \frac{1}{G_{PNN}} + \frac{qr_{PD}P_{opt}R_L}{2G_{PNN}kT} + \frac{P_{opt}^2r_{PD}^2R_LRIN}{4G_{PNN}kT} \quad (12)$$

Such as RF link loss, the RF noise figure of the simulated PNN architectures, shown in **Figure 6**, exhibits optimal operating optical power points. The left dashed black line represents the noise figure limit due to thermal noise for DM architectures, and the right dashed black line represents the noise figure limit due to RIN and nonlinear waveguide loss for EM architectures. The DM architecture exhibits a 22.52 dB noise figure at 0 dBm optical power. The EM PNN architecture exhibits a noise figure of 35.84 dB and 37.22 dB at 20.4 dBm optical power for off-chip and on-chip modulation, respectively. The DM PNN architecture has an optimal noise figure of 22.52 dB at 0 dBm optical power and significantly outperforms the single-ended EM PNN architectures by 13.32 dB at optimal operating points. The difference in performance is due to the DM architecture optimally performing within the thermal noise limited region, while the high gain

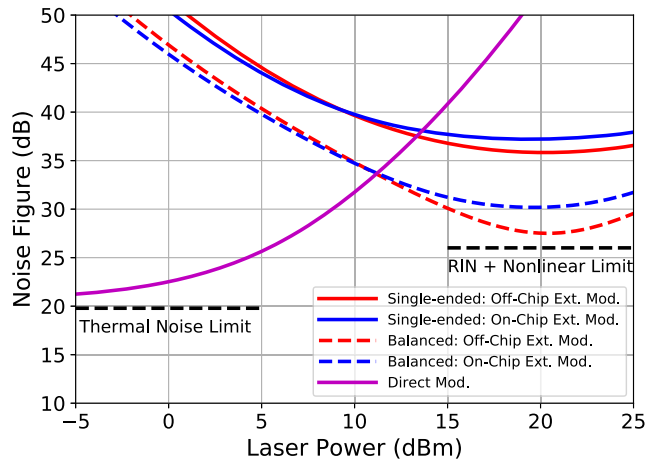


Figure 6. RF noise figure of the linear front-end of the PNN as a function of optical power for different modulation architectures. Left dashed black line indicates noise figure limit for DML dominated by thermal noise. Right dashed black line indicates noise figure limit for EM architecture limited by RIN and nonlinearity within the waveguide.

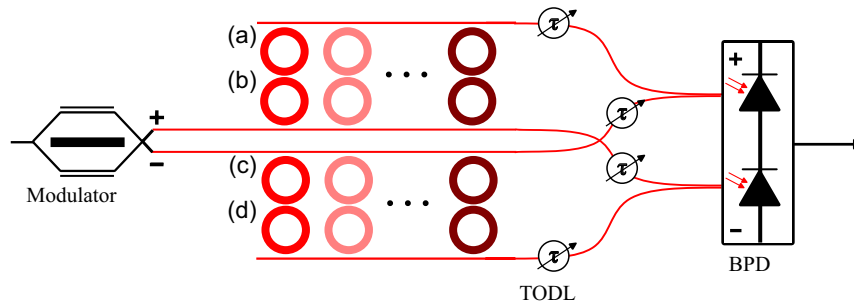


Figure 7. Schematic for novel balanced weight bank architecture for reduction in noise within the linear front-end of the PNN. a–d) correspond to the four unique optical paths referenced within Equation (13) and (14). TODL = tunable optical delay line, BPD = balanced photodetectors.

region for EM PNN architectures is within the RIN limited region, which is a higher noise power term.

5.4. Balanced Weight Bank

First introduced to improve the noise figure of fiber-based analog photonic links, differential detection links, also known as balanced architectures, implement a dual-output MZM (DO-MZM) to generate complementary RF signals on two matched optical paths terminated by a BPD.^[46] The complementary signals add, resulting in 6 dB RF gain compared to single-ended links, and simultaneously the common-mode laser noise, RIN, subtracts. The amount of RIN power removed is proportional to the precision of the matching between the two optical paths with respect to amplitude and phase as well as inversely proportional to the amount of RF power into the DO-MZM.^[30] By suppressing RIN, the noise figure of EM architectures can be significantly decreased by extending the shot noise-limited region. Within this region, increased optical power results in squared RF gain while only linearly increasing noise; therefore, the noise figure will be reduced linearly. This technique can be implemented in the input layer of the PNN weight bank in the configuration shown in **Figure 7**, creating a balanced weight bank, first purposed in ref. [28]. Double-ring MRRs are implemented to better match the four optical path lengths to improve RIN suppression and weighting accuracy.

The balanced weight bank reduces the noise figure of the EM architectures by 7.04 and 8.33 dB for off-chip and on-chip modulation, respectively. For applications which require modulation bandwidths higher than DM can support, this architectural type can preserve RF performance at high speeds. The caveat to implementing this architecture is the increased complexity in control and the number of devices. This increase in control complexity could reduce the precision of the weight bank, which can negatively impact classification performance depending on application requirements.^[19,20] For the RF simulations, 30 dB of RIN suppression was assumed,^[30] and the performance of the balanced links is shown by dashed curves. Equation (13) and (14) show the necessary MRR weight control required to achieve the desired weight required by the PNN while still optimizing for the suppression of RIN. As shown in Equation (14), the RIN noise terms $n_{RIN}(t)$ are canceled out while the modulated optical signal, $X(t)$, experiences a factor of two gain. The ring

weighting term, α , is mapped to the desired weighting term, w , by the final relationship in Equation (14).

$$\begin{aligned} [a]: & \alpha(X(t) + n_{\text{RIN}}(t)) & [c]: & (1 - \alpha)(-X(t) + n_{\text{RIN}}(t)) \\ [b]: & (1 - \alpha)(X(t) + n_{\text{RIN}}(t)) & [d]: & \alpha(-X(t) + n_{\text{RIN}}(t)) \end{aligned} \quad (13)$$

$$\begin{aligned} \text{RF Out: } wX(t) &= [1+3] - [2+4] \\ &= [X(t)(2\alpha - 1) + n_{\text{RIN}}(t)] - [X(t)(-2\alpha + 1) + n_{\text{RIN}}(t)] \\ &= 2X(t)[2\alpha - 1] \\ w &= [2\alpha - 1] \end{aligned} \quad (14)$$

5.5. Low Noise Amplification

Pre-amplification is critical within MWP systems. With this technique, the input signal SNR is improved before the introduction of optical noise. LNA simply decreases the RF link loss by the gain of the amplifier and reduces the noise figure by the Friis equation for series noise stages, Equation (15). The caveat of pre-amplification is the reduction in the system's maximum RF power handling, third-order intercept point (IIP3), by a factor of the pre-amplifier gain. Additionally, excess power consumption of the amplifier will reduce overall compute efficiencies.

A COTS ultra-wideband LNA, RLNA05M54GA, was implemented for the following simulations with gain of 23 dB and noise figure of 4 dB (Figure 8). The link loss improvement due to the implementation of LNA is equal to the gain of the LNA. The noise figure of the DM PNN architecture was improved by 17.2 dB at 0 dBm optical power. The EM PNN architecture was improved to 21.3 and 20.24 dB noise figure at optimal optical input power for the off-chip and on-chip, respectively.

$$F_{\text{LNA+PNN}} = F_{\text{LNA}} + \frac{F_{\text{PNN}} - 1}{G_{\text{LNA}}} \quad (15)$$

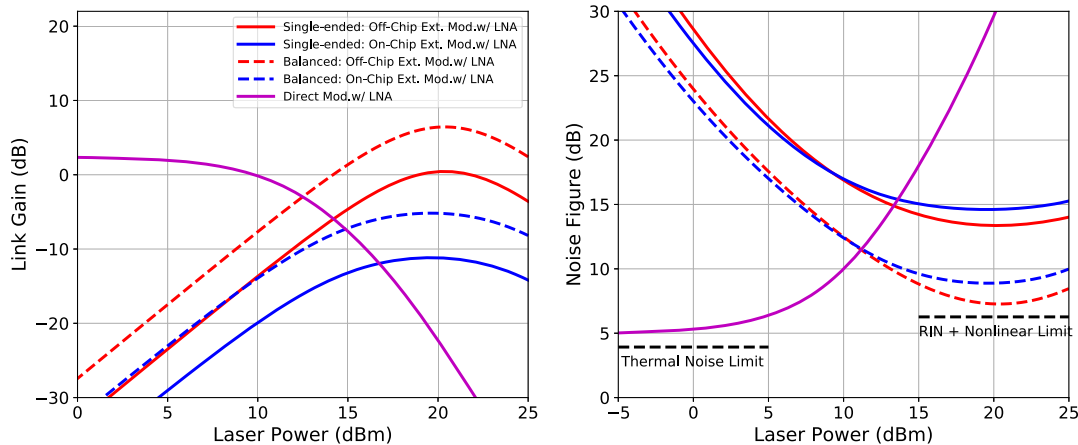


Figure 8. RF link loss (left) and noise figure (right) of the linear front-end of the PNN with the inclusion of a low-noise amplifier as function of optical power for different modulation architectures.

5.6. Spurious Free Dynamic Range Analysis

Finally, the PNN architectures were simulated with respect to SFDR to determine the range of signal powers that can be processed. SFDR is defined by the difference between the lower power limit, the MDS, and the upper power limit, IIP3. The IIP3 is defined as the RF input power in which intermodulation distortion products (IMD) begin to dominate. Regarding the photonic systems presented, the third-order IMD dominates and therefore will be the focus of this analysis.^[3] The MDS is defined as the thermal noise floor plus the noise figure of the system. SFDR analysis provides insight into performance metrics trade-offs and should therefore be optimized for specific application needs (Figure 9).

$$\text{IIP3}_{\text{EM}} = \frac{4V_{\pi}^2}{\pi^2 R_L} \quad (16)$$

$$\text{IIP3}_{\text{DM}} = 10 \times \log_{10} \left(\frac{c_{\text{DML}} \times P_{\text{opt}}^2 \times R_L}{2 \times S_{\text{LD}}} \right) \quad (17)$$

$$\begin{aligned} \text{SFDR}_{2/3} &= (2/3)(\text{IIP3} + \text{MDS}) \\ &= (2/3)(\text{IIP3} + \text{NF} + 174) \end{aligned} \quad (18)$$

As shown in the previous analysis sections, operating a DM architecture at low power levels is advantageous for noise figure. Although beneficial for noise figure, low-power operation of DM links can reduce SFDR due to an increase in nonlinearity caused by clipping of the input signal.^[29,47,48] To avoid this effect, a DM link will experience full linearity above 10 mW input power.^[29,48] Alternatively, the system can operate below this optical limit, but the electrical input must be limited to small signals, where the amplitude of the modulated signal, I_m , is within the bounds of the difference in current bias, I_{Bias} , and current threshold, I_{th} , as shown in Equation (19).^[29] Research in predistortion amplifiers to compensate for clipping can enable the operation of DM links without a large reduction in SFDR.^[49]

$$I_m = m(I_{\text{Bias}} - I_{\text{th}})/2, 0 \leq m \leq 1 \quad (19)$$

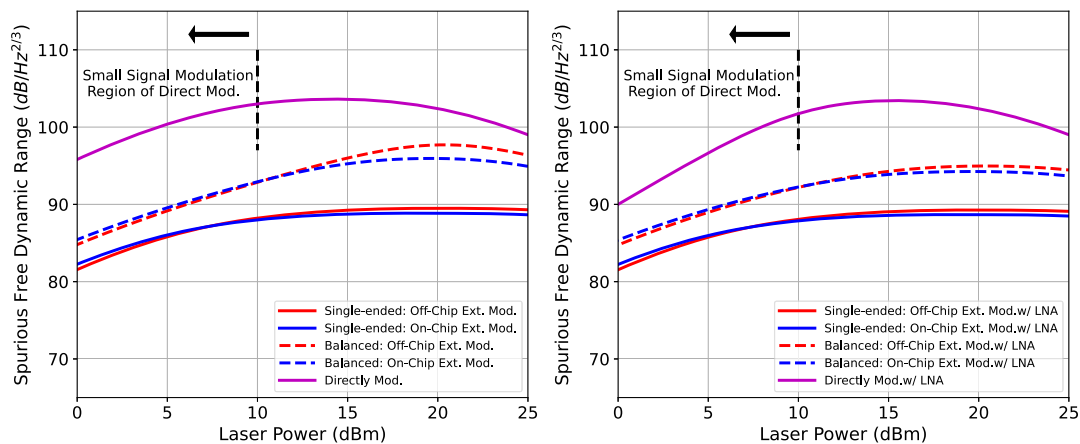


Figure 9. SFDR of the linear front-end of the PNN with (right) and without (left) the inclusion of a low-noise amplifier as a function of optical power for different modulation architectures.

The DM system outperforms EM architectures with respect to third-order SFDR achieving $103.4 \text{ dB Hz}^{-2/3}$ at 15.3 dBm optical power. While this operating point is optimal for dynamic range, noise figure and link loss suffer. Unlike the DM PNN architecture, the optimal operating point for EM architectures is optimal at 20.4 dBm optical power across all RF metrics, resulting in less critical trade-offs.

6. Conclusion

As neuromorphic photonic technologies mature, operating frequencies will continue to scale proportionally, resulting in a critical need for more in-depth RF performance-focused analysis, evaluation, and design. These efforts will ensure that PNN performance is maintained as the reach of this technology expands further throughout the wireless spectrum.

High-speed linear operation of silicon neuromorphic photonic systems was demonstrated via wideband linear weighted summation. These results demonstrated a 3 dB weighting bandwidth of 4.7 GHz with a 0.1 dB variation between the weighting values. These results highlighted the trade-offs between instantaneous bandwidth and channel count within the MRR design. Furthermore, these results highlighted the analogous nature of high-speed PNN operation to that of MWP cancellation systems, and therefore, the need for highly precise path matching to maintain weighting accuracy as operating bandwidth increases.

Additionally, a key insight generated in this work was that the overall noise performance of a PNN is determined by the noise figure of the input layer. Following this first decision, nonlinear operations preserve noise performance^[22] and only link loss must be compensated for. RF amplification within the O-E-O link of the photonic neuron can compensate for such losses and enable scalability. Therefore, RF optimization of PNNs serves two goals. First, minimize the noise figure of the linear front-end to improve classification in noisy wireless environments. Second, reduce the link loss of photonic neurons throughout the network to minimize the gain requirements of electrical amplification responsible for ensuring scalability. Further

evaluation of the input layer highlighted that current single-ended EM PNN architectures, which are often deployed, are a poor choice due to the high noise figure.

The RF analysis section investigated RF performance with respect to link loss, noise figure, and SFDR for five potential architectures. The analysis utilized current state-of-the-art commercially available devices. By implementing the nonlinear waveguide loss mechanisms within the silicon waveguide and MRR due to TPA and FCA, optimal optical power operating points were extracted for each architecture. Furthermore, the implementation of LNA was explored to significantly improve link loss and noise figure at the cost of IIP3. Finally, to address the high noise figure of the EM PNN architectures, a balanced weight bank was explored to suppress RIN with the caveat of doubling the complexity of weight bank control.

The conclusions of the RF analysis are convoluted and one architecture does not outperform all other architectures with respect to all metrics. For minimal link loss, a balanced EM PNN linear front-end achieves 16.56 dB loss at 20.4 dBm optical power, further improved by the gain of a low-noise amplifier. For a minimal noise figure, a DM PNN linear front-end achieves 22.52 dB at 0 dBm optical power. These optimized architectures outperform the traditional EM PNN on-chip input layer by 17.6 dB reduced loss and 14.7 dB reduced noise figure. The DM architecture performs optimally at low powers with respect to noise figure, which makes this architecture an excellent candidate for full cointegration with on-chip active lasers, which are usually power limited.^[50,51] Although the DM architecture performs well at low powers, the SFDR of the PNN at this point suffers from the effects of clipping. This mismatch between the noise figure and the SFDR optimal operating points motivates the use of balanced EM architecture, which has a well-matched optimal operating point across all the RF performance metrics of interest.

In conclusion, RF analysis of silicon PNNs provides insights into optimizing RF performance by architectural design decisions and optimal operating points. This information empowers the designer to develop PNNs that reflect the specific needs of the application. The RF performance improvements gained through

optimization result in a broadening of the application space in which neuromorphic photonics can be deployed.

Acknowledgements

The authors would like to acknowledge and thank the support of the National Science Foundation for supporting this work under the Spectrum and Wireless Innovation enabled by Future Technologies (SWIFT) (grant no. 2128616). S.B. acknowledges funding from the Fonds de recherche du Québec Nature et technologies.

Conflict of Interest

The authors declare no conflict of interest.

Data Availability Statement

The data that support the findings of this study are available from the corresponding author upon reasonable request.

Keywords

broadband processing, neuromorphic photonics, radio frequency photonics, silicon photonics

Received: October 25, 2023

Revised: February 20, 2024

Published online:

- [1] J. Capmany, D. Novak, *Nat. Photonics* **2007**, *1*, 319.
- [2] A. J. Seeds, K. J. Williams, *J. Lightwave Technol.* **2006**, *24*, 4628.
- [3] C. H. Cox, E. I. Ackerman, G. E. Betts, J. L. Prince, *IEEE Trans. Microwave Theory Tech.* **2006**, *54*, 906.
- [4] E. I. Ackerman, C. H. Cox, in *Microwave Photonics (MWP) and the 2014 9th Asia-Pacific Microwave Photonics Conf. (APMP) 2014*, Int. Topical Meeting on IEEE, Hokkaido, Japan, October **2014**, pp. 430–433.
- [5] D. Marpaung, J. Yao, J. Capmany, *Nat. Photonics* **2019**, *13*, 80.
- [6] A. N. Tait, A. X. Wu, T. F. De Lima, E. Zhou, B. J. Shastri, M. A. Nahmias, P. R. Prucnal, *IEEE J. Sel. Top. Quantum Electron.* **2016**, *22*, 312.
- [7] A. Tait, T. F. De Lima, M. Nahmias, B. Shastri, P. Prucnal, *CLEO: Science and Innovations*, Optica Publishing Group, San Jose, CA, May **2018**, p. STh3B–1.
- [8] M. A. Nahmias, A. N. Tait, B. J. Shastri, T. F. De Lima, P. R. Prucnal, *Opt. Express* **2015**, *23*, 26800.
- [9] A. N. Tait, T. F. De Lima, E. Zhou, A. X. Wu, M. A. Nahmias, B. J. Shastri, P. R. Prucnal, *Sci. Rep.* **2017**, *7*, 7430.
- [10] D. Psaltis, N. Farhat, *Opt. Lett.* **1985**, *10*, 98.
- [11] N. H. Farhat, D. Psaltis, A. Prata, E. Paek, *Appl. Opt.* **1985**, *24*, 1469.
- [12] B. J. Shastri, A. N. Tait, T. Ferreira de Lima, W. H. P. Pernice, H. Bhaskaran, C. D. Wright, P. R. Prucnal, *Nat. Photonics* **2021**, *15*, 102.
- [13] H.-T. Peng, J. Lederman, L. Xu, T. F. de Lima, C. Huang, B. Shastri, D. Rosenbluth, P. Prucnal (Preprint), arXiv: 2106.13865, v1, submitted: June, 2021.
- [14] H.-T. Peng, J. C. Lederman, L. Xu, T. F. De Lima, C. Huang, B. J. Shastri, D. Rosenbluth, P. R. Prucnal, *IEEE J. Sel. Top. Quantum Electron.* **2022**, *28*, 1.
- [15] C. Huang, S. Fujisawa, T. Ferreira de Lima, A. N. Tait, E. C. Blow, Y. Tian, S. Bilodeau, A. Jha, F. Yaman, H.-T. Peng, H. G. Batshon, B. J. Shastri, Y. Inada, T. Wang, P. R. Prucnal, *Nat. Electron.* **2021**, *4*, 837.
- [16] Y. Shen, N. C. Harris, S. Skirlo, M. Prabhu, T. Baehr-Jones, M. Hochberg, X. Sun, S. Zhao, H. Larochelle, D. Englund, M. Soljačić, *Nat. Photonics* **2017**, *11*, 441.
- [17] A. N. Tait, T. Ferreira de Lima, M. A. Nahmias, H. B. Miller, H.-T. Peng, B. J. Shastri, P. R. Prucnal, *Phys. Rev. Appl.* **2019**, *11*, 064043.
- [18] A. Jha, T. F. De Lima, H. Saeidi, S. Bilodeau, A. N. Tait, C. Huang, S. Abbaslou, B. Shastri, P. R. Prucnal, *Opt. Express* **2020**, *28*, 11692.
- [19] W. Zhang, C. Huang, H.-T. Peng, S. Bilodeau, A. Jha, E. Blow, T. F. De Lima, B. J. Shastri, P. Prucnal, *Optica* **2022**, *9*, 579.
- [20] T. Ferreira de Lima, E. A. Doris, S. Bilodeau, W. Zhang, A. Jha, H.-T. Peng, E. C. Blow, C. Huang, A. N. Tait, B. J. Shastri, P. R. Prucnal, *Nanophotonics* **2022**, *11*, 3805.
- [21] P. R. Prucnal, B. J. Shastri, *Neuromorphic Photonics*, CRC Press, London, UK **2017**.
- [22] T. F. De Lima, A. N. Tait, H. Saeidi, M. A. Nahmias, H.-T. Peng, S. Abbaslou, B. J. Shastri, P. R. Prucnal, *IEEE J. Sel. Top. Quantum Electron.* **2020**, *26*, 1.
- [23] K. Giewont, S. Hu, B. Peng, M. Rakowski, S. Rauch, J. C. Rosenberg, A. Sahin, I. Stobert, A. Stricker, K. Nummy, F. A. Anderson, J. Ayala, T. Barwicz, Y. Bian, K. K. Dezfulian, D. M. Gill, T. Houghton, *IEEE J. Sel. Top. Quantum Electron.* **2019**, *25*, 1.
- [24] A. Tait, T. F. De Lima, M. Chang, M. Nahmias, B. Shastri, P. Prucnal, in *2017, IEEE Optical Interconnects Conf. (OI)*. IEEE, Sante Fe, NM, June **2017**, pp. 25–26.
- [25] A. Tait, M. Nahmias, B. Shastri, M. Chang, A. Wu, E. Zhou, E. Blow, T. F. De Lima, B. Wu, P. Prucnal, In *2015, IEEE Summer Topicals Meeting Series (SUM)*, IEEE, Nassau, Bahamas, July **2015**, pp. 110–111.
- [26] M. P. Chang, M. Fok, A. Hofmaier, P. R. Prucnal, *IEEE Microwave Wireless Compon. Lett.* **2013**, *23*, 99.
- [27] J. Cardenas, M. A. Foster, N. Sherwood-Droz, C. B. Poitras, H. L. R. Lira, B. Zhang, A. L. Gaeta, J. B. Khurgin, P. Morton, M. Lipson, *Opt. Express* **2010**, *18*, 26525.
- [28] E. C. Blow, T. F. de Lima, H.-T. Peng, W. Zhang, C. Huang, B. J. Shastri, P. R. Prucnal, in *AI and Optical Data Sciences III*, Vol. 12019, SPIE, San Francisco, CA, USA, March **2022**, pp. 157–162.
- [29] C. H. Cox, *Analog Optical Links: Theory and Practice*, Cambridge University Press **2006**.
- [30] D. A. I. Marpaung, *Ph.D. Thesis*, University of Twente **2009**.
- [31] J. Bass, H. Tran, W. Du, R. Soref, S.-Q. Yu, *Opt. Express* **2021**, *29*, 30844.
- [32] J. Bass, B. Brea, H. Tran, W. Du, R. Soref, S.-Q. Yu, in *Silicon Photonics XV*, Vol. 11285, SPIE, San Francisco, CA, February **2020**, pp. 216–223.
- [33] A. N. Tait, *Phys. Rev. Appl.* **2022**, *17*, 054029.
- [34] E. L. Wooten, K. M. Kissa, A. Yi-Yan, E. J. Murphy, D. A. Lafaw, P. F. Hallemeier, D. Maack, D. V. Attanasio, D. J. Fritz, G. J. Mcbrien, D. E. Bossi, *IEEE J. Sel. Top. Quantum Electron.* **2000**, *6*, 69.
- [35] A. Samani, M. Chagnon, D. Patel, V. Veerasubramanian, S. Ghosh, M. Osman, Q. Zhong, D. V. Plant, *IEEE Photonics J.* **2015**, *7*, 1.
- [36] S. Y. Siew, B. Li, F. Gao, H. Y. Zheng, W. Zhang, P. Guo, S. W. Xie, A. Song, B. Dong, L. W. Luo, C. Li, X. Luo, G.-Q. Lo, *J. Lightwave Technol.* **2021**, *39*, 4374.
- [37] Y. Matsui, T. Pham, W. A. Ling, R. Schatz, G. Carey, H. Daghighian, T. Sudo, C. Roxlo, in *Optical Fiber Communication Conf.*, Optica Publishing Group, Anaheim, CA, March **2016**, p. Th5B–4.
- [38] R. Soref, B. Bennett, *IEEE J. Quantum Electron.* **1987**, *23*, 123.

- [39] G. T. Reed, G. Mashanovich, F. Y. Gardes, D. J. Thomson, *Nat. Photonics* **2010**, 4, 518.
- [40] M. Tokushima, J. Ushida, T. Nakamura, *Appl. Phys. Express* **2021**, 14, 122008.
- [41] L. Zhang, Y. Li, Y. Hou, Y. Wang, M. Tao, B. Chen, Q. Na, Y. Li, Z. Zhi, X. Liu, X. Li, F. Gao, X. Luo, G.-Q. Lo, J. Song, *Opt. Express* **2021**, 29, 29755.
- [42] A. F. Oskooi, D. Roundy, M. Ibanescu, P. Bermel, J. D. Joannopoulos, S. G. Johnson, *Comput. Phys. Commun.* **2010**, 181, 687.
- [43] M. M. P. Fard, G. Cowan, O. Liboiron-Ladouceur, *Opt. Express* **2016**, 24, 27738.
- [44] R. Selim, R. Hoofman, M. Khoder, A. Masood, C. Littlejohns, D. Geuzebroek, R. Grootjans, T. Drischel, K. Torki, in *Emerging Applications in Silicon Photonics II*, Vol. 11880, SPIE Photonex, Glasgow, UK, September **2021**, pp. 15–23.
- [45] N. M. Fahrenkopf, C. McDonough, G. L. Leake, Z. Su, E. Timurdogan, D. D. Coolbaugh, *IEEE J. Sel. Top. Quantum Electron.* **2019**, 25, 1.
- [46] E. I. Ackerman, G. E. Betts, W. K. Burns, J. C. Campbell, C. H. Cox, N. Duan, J. L. Prince, M. D. Regan, H. V. Rousell, in *2007 IEEE/MTT-S Int. Microwave Symp.*, IEEE, Honolulu, HI, June **2007**, pp. 51–54.
- [47] R. Sabella, M. Paciotti, A. Di Fonzo, in *Conf. Proceedings LEOS'96 9th Annual Meeting IEEE Lasers and Electro-Optics Society*, Vol. 2, IEEE, Boston, MA, November **1996**, pp. 406–407.
- [48] S. A. Khwandah, J. P. Cosmas, I. A. Glover, P. I. Lazaridis, N. R. Prasad, Z. D. Zaharis, *IEEE Photonics J.* **2015**, 7, 1.
- [49] C. Han, S.-H. Cho, M. Sung, H. S. Chung, J. H. Lee, *ETRI J.* **2016**, 38, 227.
- [50] C. Op De Beeck, B. Haq, L. Elsinger, A. Gocalinska, E. Pelucchi, B. Corbett, G. Roelkens, B. Kuyken, *Optica* **2020**, 7, 386.
- [51] J. J. van der Tol, Y. Jiao, K. A. Williams, in *Semiconductors and Semimetals*, Vol. 99, Elsevier, Amsterdam, Netherlands **2018** pp. 189–219.
- [52] J. Zhou, J. Wang, L. Zhu, Q. Zhang, *J. Lightwave Technol.* **2020**, 38, 272.
- [53] EOSPACE, *High-Performance, Low-Vpi, 20GHz Small-Form-Factor Lithium Niobate Optical Modulator*, Rev. 1, EOSPACE Inc., Redmond, WA **2014**.
- [54] APIC Corporation, *Highly Linear, Direct Modulated DFB Laser Module*, Rev. 1, APIC Corporation, Culver City, CA, USA **2018**.
- [55] J. Meitzner, F. G. Moore, B. M. Tillotson, S. D. Kevan, G. L. Richmond, *Appl. Phys. Lett.* **2013**, 103, 9.